Research Article | Vol. 25, No. 10 | 15 May 2017 | OPTICS EXPRESS 10828

Optics EXPRESS

Plasmonic nanoantenna design and fabrication based on evolutionary optimization

THORSTEN FEICHTNER,[1,2,*] OLEG SELIG,[1,3] AND BERT HECHT[1]

[1]*Nano-Optics & Biophotonics Group, Department of Experimental Physics 5, Röntgen Research Center for Complex Material Research (RCCM), Physics Institute, University of Würzburg, Am Hubland, D-97074 Würzburg, Germany*
[2]*Helmholtz-Zentrum Berlin für Materialien und Energie, Institute Nanoarchitectures for Energy Conversion, Hahn-Meitner-Platz 1, D-14109 Berlin, Germany*
[3]*Now at: FOM Institute AMOLF, Biomolecular Photonics Group, Science Park 104, 1098 XG Amsterdam, The Netherlands*
[*]*thorsten.feichtner@physik.uni-wuerzburg.de*

Abstract: Nanoantennas can tailor light-matter interaction for optical communication, sensing, and spectroscopy. Their design is inspired by radio-frequency rules which partly break down at optical frequencies. Here we find unexpected nanoantenna designs exhibiting strong light localization and enhancement by using a general and scalable evolutionary algorithm based on FDTD simulations that also accounts for geometrical fabrication constraints. The resulting nanoantennas are "printed" directly by focused-ion beam milling and their fitness ranking is validated experimentally by two-photon photoluminescence. We find the best antennas' operation principle deviating from that of classical radio wave-inspired designs. Our work sets the stage for a widespread application of evolutionary optimization in nano photonics.

OCIS codes: (250.5403) Plasmonics; (220.4241) Nanostructure fabrication;(250.5230) Photoluminescence.

References and links

1. C. A. Balanis, "Antenna theory: A review," Proceedings of the IEEE **80**, 7–23 (1992).
2. L. Novotny and N. van Hulst, "Antennas for light," Nat. Photon. **5**(2), 83–90 (2011).
3. P. Biagioni, J.-S. Huang, and B. Hecht, "Nanoantennas for visible and infrared radiation," Rep. Prog. Phys. **75**(2), 024402 (2012).
4. A. P. A.F. Koenderink, A. Alu, "Nanophotonics: shrinking light-based technology," Science **348**(6234), 516–521 (2015).
5. S. A. Maier, *Plasmonics: fundamentals and applications* (Springer, 2007)
6. J. Dorfmüller, R. Vogelgesang, W. Khunsin, C. Rockstuhl, C. Etrich, and K. Kern, "Plasmonic nanowire antennas: experiment, simulation, and theory," Nano Lett. **10**(9), 3596–3603 (2010).
7. J. Zhou, T. Koschny, M. Kafesaki, E. N. Economou, J. B. Pendry, and C. M. Soukoulis, "Saturation of the Magnetic Response of Split-Ring Resonators at Optical Frequencies," Phys. Rev. Lett. **95**(22), 223902 (2005).
8. N. Zhou, X. Xu, A. T. Hammack, B. C. Stipe, K. Gao, W. Scholz, and E. C. Gage, "Plasmonic near-field transducer for heat-assisted magnetic recording," Nanophotonics **3**(3), 141–155 (2014).
9. L. Novotny, "Effective Wavelength Scaling for Optical Antennas," Phys. Rev. Lett. **98**(26), 266802 (2007).
10. A. G. Curto, G. Volpe, T. H. Taminiau, M. P. Kreuzer, R. Quidant, and N. F. van Hulst, "Unidirectional Emission of a Quantum Dot Coupled to a Nanoantenna," Science **329**(5994), 930–933 (2010).
11. A. Alu and N. Engheta, "Wireless at the nanoscale: optical interconnects using matched nanoantennas," Phys. Rev. Lett. **104**(21), 213902 (2010).
12. J. N. Anker, W. P. Hall, O. Lyandres, N. C. Shah, J. Zhao, and R. P. Van Duyne, "Biosensing with plasmonic nanosensors," Nat. Mat. **7**(6), 442–453 (2008).
13. N. Liu, M. L. Tang, M. Hentschel, H. Giessen, and a. P. Alivisatos, "Nanoantenna-enhanced gas sensing in a single tailored nanofocus," Nat. Mat. **10**(8), 631–636 (2011).
14. M. D. Wissert, K. S. Ilin, M. Siegel, U. Lemmer, and H.-J. Eisler, "Nanoantenna-enhanced ultrafast nonlinear spectroscopy of a single gold nanoparticle," Nat. Comm. **2**, 333 (2011).
15. K. B. Crozier, W. Zhu, D. Wang, S. Lin, M. D. Best, and J. P. Camden, "Plasmonics for surface enhanced raman scattering: Nanoantennas for single molecules," IEEE Journal of Selected Topics in Quantum Electronics **20**(3), 1–11 (2014).
16. T. Feichtner, O. Selig, M. Kiunke, and B. Hecht, "Evolutionary optimization of optical antennas," Phys. Rev. Lett. **109**, 127701 (2012).

#286492 https://doi.org/10.1364/OE.25.010828
Journal © 2017 Received 16 Feb 2017; accepted 19 Feb 2017; published 2 May 2017

Optics EXPRESS

17. C. Forestiere, M. Donelli, G. F. Walsh, E. Zeni, G. Miano, L. Dal Negro, and L. D. Negro, "Particle-swarm optimization of broadband nanoplasmonic arrays," Opt. Lett. **35**(2), 133–135 (2010).
18. C. Forestiere, A. J. Pasquale, A. Capretti, G. Miano, A. Tamburrino, S. Y. Lee, B. M. Reinhard, and L. Dal Negro, "Genetically Engineered Plasmonic Nanoarrays," Nano Lett. **12**(4), 2037–2044 (2012).
19. P. Ginzburg, N. Berkovitch, A. Nevet, I. Shor, and M. Orenstein, "Resonances On-Demand for Plasmonic Nano-Particles," Nano Lett. **11**(6), 2329–2333 (2011).
20. C. Forestiere, Y. He, R. Wang, R. M. Kirby, and L. Dal Negro, "Inverse Design of Metal Nanoparticles' Morphology," ACS Phot. **1**(3), 68–78 (2015).
21. S. N. Sivanandam and S. N. Deepa, *Introduction to Genetic Algorithms* (Springer-Verlag Berlin Heidelberg, 2008).
22. J.-S. Huang, V. Callegari, P. Geisler, C. Brüning, J. Kern, J. C. Prangsma, X. Wu, T. Feichtner, J. Ziegler, P. Weinmann, M. Kamp, A. Forchel, P. Biagioni, U. Sennhauser, and B. Hecht, "Atomically flat single-crystalline gold nanostructures for plasmonic nanocircuitry," Nat. Comm. **1**, 150 (2010).
23. R. Fernández-García, Y. Sonnefraud, A. I. Fernández-Domínguez, V. Giannini, and S. A. Maier, "Design considerations for near-field enhancement in optical antennas," Contemp. Phys. **55**(1), 1–11 (2014).
24. C. Rockstuhl, F. Lederer, C. Etrich, T. Zentgraf, J. Kuhl, and H. Giessen, "On the reinterpretation of resonances in split-ring-resonators at normal incidence," Opt. Express **14**(19), 8827–8836 (2006).
25. A. García-Etxarry, P. Apell, M. Käll, and J. Aizpurua, "A combination of concave / convex surfaces for field-enhancement optimization : the indented nanocone," Opt. Express **20**(23), 1111–1116 (2012).
26. J.-S. Huang, J. Kern, P. Geisler, P. Weinmann, M. Kamp, A. Forchel, P. Biagioni, and B. Hecht, "Mode Imaging and Selection in Strongly Coupled Nanoantennas," Nano Lett. **10**(6), 2105–2110 (2010).
27. K. Imura, T. Nagahara, and H. Okamoto, "Near-Field Two-Photon-Induced Photoluminescence from Single Gold Nanorods and Imaging of Plasmon Modes," J. Phys. Chem. B **109**(27), 13214–13220 (2005).
28. M. D. Wissert, K. S. Ilin, M. Siegel, U. Lemmer, and H.-J. Eisler, "Coupled nanoantenna plasmon resonance spectra from two-photon laser excitation," Nano Lett. **10**(10), 4161–4165 (2010).
29. P. G. Etchegoin, E. C. Le Ru, and M. Meyer, "An analytic model for the optical properties of gold," J. Chem. Phys. **125**(16), 164705 (2006).
30. P. G. Etchegoin, E. C. Le Ru, and M. Meyer, "Erratum: An analytic model for the optical properties of gold," J. Chem. Phys. **127**(18), 189901 (2007).
31. T. Feichtner, O. Selig, M. Kiunke, and B. Hecht, figshare (2017) [retrieved 20 February 2017], https://doi.org/10.6084/m9.figshare.4669009

1. Introduction

Ideas from radio frequency technology, where oscillating currents are transduced into electromagnetic radiation and vice versa [1] can also be applied to realize antennas for light [2, 3], which can be used to enhance light-matter interaction on the nano-scale [4]. However, for such very high frequencies many established concepts of antenna theory need to be adapted. For example the occurrence of plasmon resonances [5] and volume currents [6] have to be considered, and new phenomena become important, e.g. the kinetic inductance [7] and Ohmic loss [8]. To rescue the concepts of radio frequency antenna technology into the optical realm the principle of effective wavelength scaling was introduced [9] and applied in optical communication [10, 11], sensing [12, 13], and spectroscopy [14, 15]. However, this approach does not always lead to the best possible antenna performance and, as we have shown before, unexpected designs found by evolutionary optimization can perform much better [16].

So far, evolutionary optimization has been applied to plasmonic systems that searched a limited parameter space, e.g. arrays of scattering discs [17, 18] as well as specifically shaped single particles [19, 20]. Here, we show how to perform evolutionary optimization of plasmonic geometries in a by far larger parameter space while taking into account topological constraints of the fabrication method. This is achieved by using smallest primitive elements ("pixels") and a set of rules that take into account geometric constraints of pixel arrangements to incorporate characteristics of the focused-ion-beam milling process. This approach guarantees that every structure that is considered during evolutionary optimization can be readily fabricated in full detail by focused ion beam (FIB) milling of a thin layer of monocrystalline gold. This allows us to experimentally investigate a hierarchy of antenna structures obtained by genetic optimization and validate their relative performance experimentally using two-photon photoluminescence. A detailed analysis of finite-difference-time-domain simulations reveals an unique operation prin-

Optics EXPRESS

ciple of the fittest antenna.

2. Evolutionary algorithm

An evolutionary algorithm (EA) is an iterative numerical technique inspired by biology to find optimized solutions of non-analytical problems [21]. It is based on inheritance of favorable properties of a valid solution (individual), which is fully described by a string of characters (genome). One iteration step consists of two parts: i) A set of individuals (generation) is evaluated with respect to its capability to solve the posed problem. The evaluation is realized by a fitness function which assigns a real number (fitness parameter) to each individual thereby creating a ranking of solutions within a generation. ii) The genome of the fittest individuals of a generation (parents) is used as source for the next generation, assembling new genomes via small random changes of parent genomes (mutation) or the combination of two parent genomes to generate a child genome (crossing).

Here we adapted our EA based on finite difference time domain (FDTD) simulations combined with a Matlab code [16] to find planar optical antennas for which the near-field localization and intensity enhancement is optimized at $\mathbf{r}_0$, the very center of the antenna. Accordingly, the fitness parameter was chosen to be the near field intensity enhancement (NFIE) polarized along the x-direction $I_x(\mathbf{r}_0) = E_x(\mathbf{r}_0)^2$, normalized to the illumination intensity without antenna.

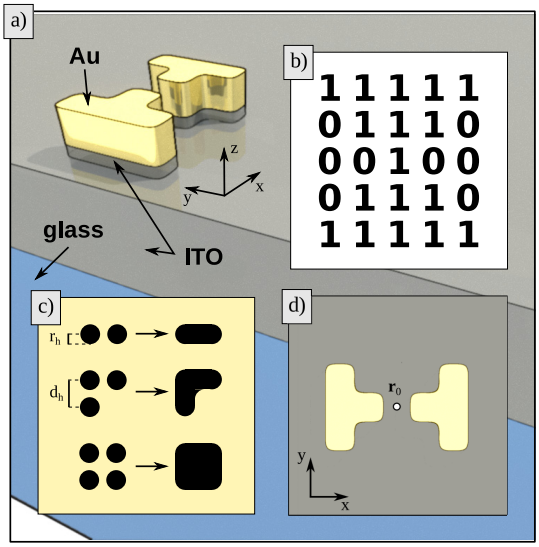

Fig. 1. Genome and geometric constraints. (a) 3D sketch of an exemplary geometry on top of an 10 nm ITO podest on an ITO layer covering a glass substrate. The rounded features occur due to FIB milling. (b) binary 5×5 genome of a small optical bow-tie-like antenna, where '1' denotes the positions at which the gold will be removed. (c) Rules for replacing neighboring hole arrangements by structures that can be fabricated by FIB. r_h: hole radius, d_h: center-to-center hole distance. (d) top view of the structure resulting from the genome in (b) after applying the rules sketched in (c). r_0 denotes the point of optimization for the NFIE.

Figure 1 illustrates the encoding and geometrical interpretation of the planar antenna structures used within the genetic algorithm. Antennas are assumed to consist of 30 nm thick gold on top of a 10 nm indium tin oxide (ITO) podest residing on 200 nm ITO on top of a glass substrate, corresponding to later experimental conditions (see Fig. 1(a)). The high transparency and the

Optics EXPRESS

good conductivity of the substrate are ideal for ion beam milling, SEM imaging, as well as optical characterization. The genome is a two dimensional square matrix with binary entries (see Fig. 1(b)). Each '1' denotes a cylindrical hole which approximates the structural primitive of FIB fabrication. As the antenna center is meant to be the area of maximum NFIE, the matrix center is always set to '1'. Figure 1(c) illustrates, how possible hole arrangements are converted to a realistic geometry that can be fabricated by FIB milling: adjacent holes are connected, leading to geometries as the one sketched in Fig. 1(d). A test pattern was devised (see Appendix 6.1) to identify the parameters for the hole radius r_h and center-to-center hole distance d_h which result in reproducible patterns when FIB milling a 30 nm thick single crystalline gold flake [22].

The evolutionary algorithm was run using a 11×11 square array with r_h = 11 nm and d_h = 30 nm. In the simulations the antenna is excited using a Gaussian focus (NA = 1.4; λ_{exc} = 830 nm) at normal incidence, centered onto the structure. The resulting overall antenna area of 330 nm×330 nm fits the FWHM of the Gaussian focus of ≈ 390 nm.

3. Results and discussion

3.1. Evolution

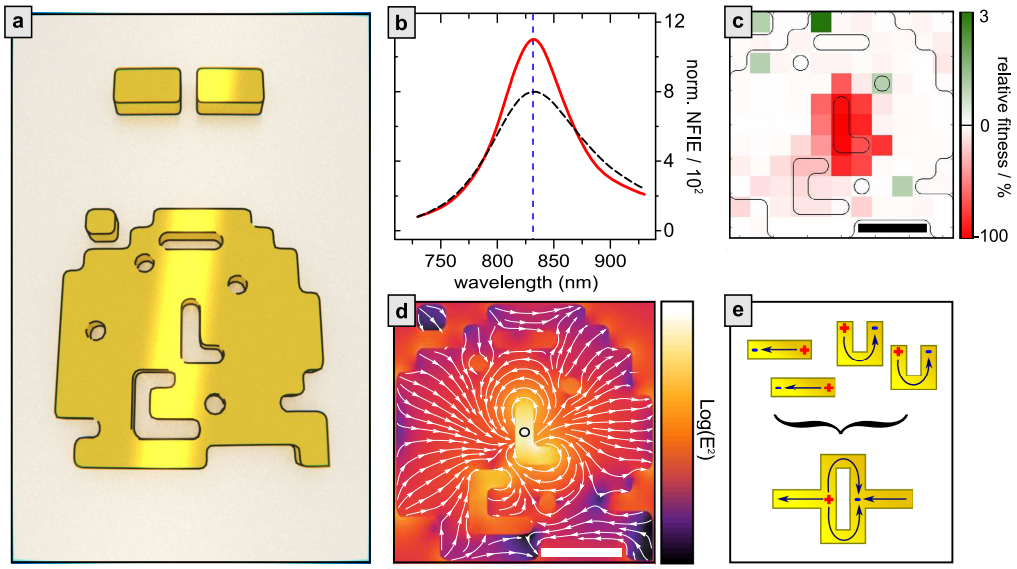

Fig. 2. Properties of the fittest evolutionary antenna (FEA): (a) 3D sketch of the reference dipolar antenna (top) and the FEA (bottom) on substrate. (b) Near field intensity enhancement (NFIE) spectrum at the very center of the reference antenna (black dashed) and the FEA (red). The optimization wavelength is marked blue. (c) Toggle plot of FEA (for details see text). (d) Near field intensity and current direction (white arrows) in the center plane of the FEA. (e) Model for the operation principle of the FEA constructively combining current patterns from two split-ring resonators and two rod antennas. All scale bars are 100 nm.

The best geometry originating from the EA (exact parameters in the methods section and Appendix 6.2), the fittest evolutionary antenna (FEA), is a compact asymmetric structure with a high filling factor of 65 % with an L-shaped gap in the very center (see lower part of Fig. 2(a)). We compare its fitness to a dipolar antenna with corresponding geometrical constraints (depicted in Fig. 2a, top), its arm dimensions being 112 × 38 × 30 nm^3 with a gap of 22 nm optimized

Optics EXPRESS

via its arm length to exhibit a near field intensity enhancement in the gap at λ = 830 nm.

The NFIE spectra of both antennas show a Lorentzian-shaped resonance with a maximum of 1100 at λ_{FEA} = 832 nm for the FEA and of 796 at λ_{res} = 830 nm for the reference antenna (see Fig. 2(b) with a full width at half maximum of $\Delta\lambda_{FEA}$ = 74 nm compared to $\Delta\lambda_{ref}$ = 107.5 nm. This corresponds to a Q-factor $Q_{FEA} = \lambda_{FEA}/\Delta\lambda_{FEA}$ = 11.2 for the FEA and $Q_{ref} = \lambda_{ref}/\Delta\lambda_{ref}$ = 7.7 for the reference antenna, respectively. As a higher Q-factor originates from lower combined radiative and ohmic losses [3], the far-field coupling of the FEA is reduced in comparison to the reference antenna. Nevertheless, the FEA exhibits an 1.4-fold higher near-field intensity enhancement in the antenna center, which further highlights its improved energy concentration mechanism.

The asymmetry of the FEA geometry originates from the still too coarse discretization provided by the antennas primitive elements: changing antenna dimensions in steps of 30 nm results in large shifts of resonance frequency making it difficult to perfectly match the optimization frequency with a symmetric geometry. The importance of individual FEA building blocks for the obtained NFIE can be assessed using a toggle plot as shown in Fig. 2(c), which visualizes the relative fitness change of 120 antenna structures with a single pixel switched from '0' → '1' or vice versa with respect to the FEA. The toggle plot clearly demonstrates that the pixels close to the center play the most important role for the antenna performance. Some green areas indicate that the FEA structure does not correspond to the absolute global maximum in the configuration space of the EA and a slight increase of near field intensity enhancement up to 3 % can be achieved by switching single elements in the periphery.

To understand the working principle of the FEA we analyze the NFIE distribution (color coded in Fig. 2(d)) and a temporal snapshot of the current pattern (white lines and arrows). The near field intensity at the optimization point (marked with circle) yields a 1100-fold normalized enhancement which is nearly fully *x*-polarized. The current pattern suggests an accumulation of charges at positions close to the optimization point within the antenna even in the absence of tip-like structures. Only the kink of the L-shaped central void contributes to the enhancement by means of the lightning rod effect, similar as in bow-tie antenna geometries [23].

The FEA current pattern can be described by a constructive superposition of two fundamental modes [16] (see Fig. 2(e)): (i) dipolar antenna currents comparable to the lowest order bonding-mode current pattern of linear two-wire antennas [3] with the well-known benefits of good far-field coupling as well as accumulation of opposite charges at either side of the gap as well as; (ii) the current pattern of fundamental split-ring like modes [24] above and below the gap, leading to additional charge accumulations at the center and resulting in a larger NFIE as for a plain dipolar antenna. A similar concept has been used to numerically optimize tips for scanning near-field optical microscopy [25].

3.2. Experiment

The FEA as well as five antenna structures from earlier generations showing a decreasing fitness were fabricated by means of focused ion beam milling of a single-crystalline gold flake [22] (see Fig. 3(a) and methods for details). To evaluate the reproducibility, each structure was fabricated six to eight times in a row, the first row denoted #1 containing the FEA.

The thickness of the structures after focused ion beam milling was measured by AFM to be 28 ± 2 nm closely matching the intended 30 nm (see Appendix 6.3). To account for the small deviation in thickness all geometries were re-simulated with decreased thickness (see Appendix 6.4) of 28 nm resulting in a slightly reduced fitness for all geometries, while preserving the hierarchy of relative fitnesses, except for a slight increase for structure #5.

Two-photon-photo-luminescence (TPPL) is used to experimentally probe the relative change of near-field intensity enhancement of the fabricated antenna structures [26]. In good approximation the intensity I_{TPPL} of the TPPL signal is proportional to the integral of the fourth power

Optics EXPRESS

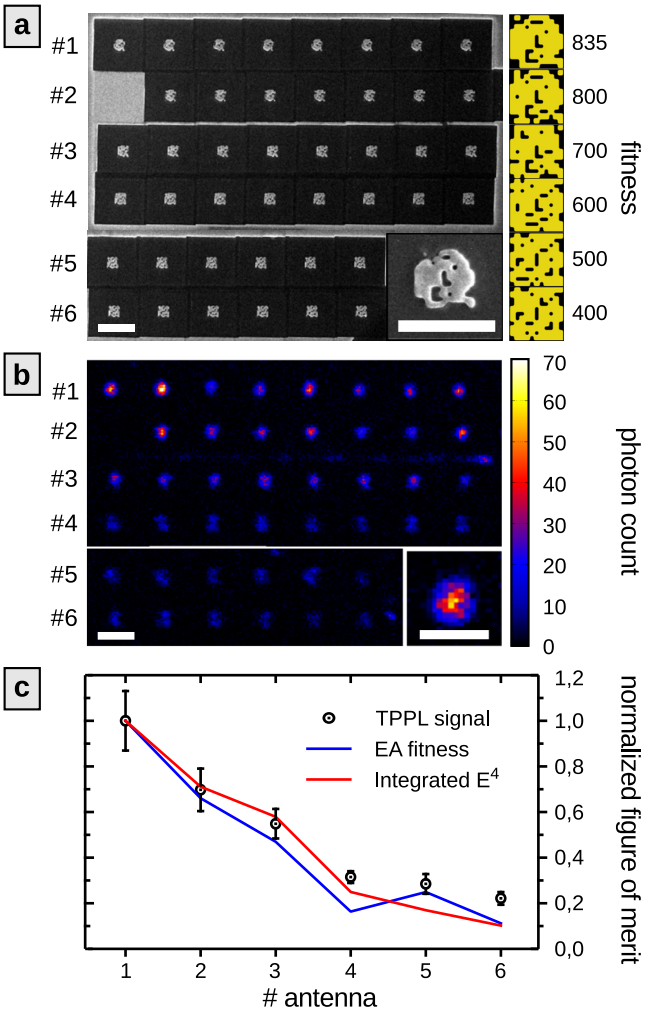

Fig. 3. Experimental realization of evolutionary antennas: (a) Exemplary SEM image of the EA antenna array realized by means of FIB milling together with geometry sketches and simulated fitness. Each row contains six to eight copies of the same geometry, the fitness decreasing from top to bottom (scale bar 1 μm). (b) TPPL map of the fabricated array (scale bar 1 μm). The insets in (a) and (b) show detailed maps of one of the very best antennas (scale bars 500 nm). (c) TPPL data (black dots) alongside with simulated fitness (near field intensity enhancement - red line) and the simulated TPPL (eq. (1) - blue line).

Optics EXPRESS

of the electrical field **E** within the volume of the antenna V_{ant} [27]:

$$I_{TPPL} \propto \int_V \mathbf{E}^4 \, dV_{ant} \quad . \tag{1}$$

Equation (1) allows to numerically calculate the relative changes of emitted TPPL signal based on simulated antenna modes [26].

Additionally, TPPL is dipole forbidden and requires strong field gradients introduced by the curvature of the nano structures, leading to vanishing signal at flat metal films. The vast majority of the signal therefore originates from the volume near the antenna hot spots, where the field gradients are largest. The fabricated EA antennas show nearly identical geometries around the central hot spot (see Fig. 3(a) left). They can therefore be compared reliably by means of TPPL, which provides a measure for the relative NFIE, assuming $I_{TPPL} \propto I_x^2(\mathbf{r}_0)$. The gap of the reference antenna strongly deviates in shape from the EA antennas and exhibits much less metal near the optimization spot. Therefore, their TPPL signals cannot be compared quantitatively (see Appendix 6.5).

TPPL of the fabricated antennas is recorded by scanning confocal microscopy using a 300 fs Ti:Sa laser at a center wavelength of 830 nm (see methods for details). Figure 3(b) shows the resulting TPPL map. The antennas are clearly distinguishable and the trend of decreasing signal for antennas with lower fitness is obvious.

Figure 3(c) shows the comparison between experimental and numerical results, assuming that the antennas have no resonance at the TPPL emission wavelengths of 500 – 680 nm. The experimental data points are acquired by integrating the TPPL count rates over the area of the individual antennas. Mean and standard deviation are calculated and normalized to the value of the FEA. As numerical results, both the simulated fitness parameter squared as well as the simulated TPPL signal (eq. (1)) for 28 nm thick antennas are plotted, each also normalized to the respective value of the FEA. There is good agreement for the relative changes of measured TPPL signal, simulated fitness and simulated TPPL signal. The trend of increasing error bars with increasing fitness can be explained by the influence of different hole sizes due to fabrication inaccuracies. The NFIE of the antennas depends heavily on the central area geometry due to the capacitive coupling across the width of the center gap (see Appendix 6.6).

For the two antennas with lowest fitness the measured normalized count rates are consistently higher than the simulated relative signal strengths. This maybe due to different effects: i) the emission of the TPPL signal could be enhanced by small antenna resonances in lower wavelength regions [28]. A numerical assessment of this effect, which seems to be very small, can be found in Appendix 6.7. ii) antennas #5 and #6 do not show a single central peak in the TPPL map. This most probably originates in the existence of multiple or higher order modes [26], not included in the simulations with the excitation focus being fixed in the very center of their geometries. However, an evaluation of the experimental data at the very center of the antennas decreased the signal-to-noise ratio but did not improve the match of simulation and experiment (see Appendix 6.8).

4. Conclusions

We established an evolutionary algorithm describing realistic planar optical antenna geometries with feature sizes of $\approx$ 22 nm that can be directly printed via FIB milling. The fittest antenna resulting from an optimization of near field intensity enhancement is a rather compact, yet complex geometry which exhibits a surprisingly clean Lorentzian resonance. The responsible mode can be described by a superposition of a dipolar antenna resonance and split ring resonances. Comparison of experimental two-photon photo luminescence data and corresponding numerical simulations show good agreement and prove the possibility to establish a direct link between

Optics EXPRESS

evolutionary optimization and fabrication of optimized structures which indeed display the expected high performance.

The presented optimization method is very flexible and can be used for arbitrary parameters, e.g. scattering direction or loss minimization, by choosing an appropriate fitness function. Also multi-objective optimization, as useful for e.g. non-linear processes or, more generalized, for experiments with both the input and output channel having predefined properties is possible. Finally, we hope that a further analysis of geometries resulting from an evolutionary algorithm leads to an improved understanding of light-matter interaction in optical antennas.

5. Materials and methods

5.1. FDTD simulations

Commercial software (FDTD Solutions, Lumerical) was used to numerically solve Maxwell's Eqs. by means of the finite-difference-time domain algorithm. For the dielectric function of gold an analytical model was used [29, 30], while the optical index for glass and ITO where set to $n = 1.4$ and $n = 2$ respectively. The fitness parameter I_x was normalized to the maximum field intensity of the Gaussian excitation without antenna but in presence of the substrate.

5.2. Evolutionary optimization

A MatLab script generates the binary matrices representing the individuals and converts them into rounded geometries within the FDTD solver according to geometrical rules (see Fig. 1). One generation of the evolutionary algorithm consists of 30 individuals and to obtain the best antenna structure a run of 60 generations has been performed. The first generation consisted of random structures with a filling factor of 0.7. The antennas were ranked according to their fitness and the best eight structures were taken as parents of the subsequent generation (more details about the mechanism of the EA can be found in [16] as well as in Appendix 6.2). Three methods were employed to create the next 30 individuals: mutation (creation of random structures), as well as linear and spiral genome crossing (see Appendix 6.2). To optimize the performance of the algorithm, each simulation was terminated after 35 fs internal simulation time. At that moment typically > 98% of electromagnetic energy has already left the simulation volume and the obtained results represent a good approximation to a fully converged simulation. This is sufficient for comparing the fitnesses of individuals within one generation of the EA while reducing the simulation time of a single individual to $\approx$ 40 min instead of $\approx$ 2h for a full simulation. All data used for quantitative evaluation and in particular all data presented in this work are retrieved from fully converged simulations.

Code availability: The code used for evolution as well as for FIB pattern generation is available online [31].

5.3. Sample substrate preparation

Microscope cover slips (Menzel, 24 $\times$ 24 mm^2, 0.17 nm thick) were covered with 200 nm of sputtered ITO. A gold marker structure was evaporated and processed by means of optical lithography. Wet-chemically grown gold flakes [22] were drop-cast and the resulting sample was plasma cleaned for 60 s in a 30 W low pressure oxygen plasma.

5.4. AFM measurements

The thickness of flakes and structures was measured at ambient conditions using tapping mode AFM operating at a resonance frequency of 240 – 280 kHz and a scanning rate of 0.2 Hz (DMLS scanning head, Nanoscope IIIa, Digital Instruments).

Optics EXPRESS

5.5. Antenna structuring

Focused ion beam (FIB) milling (Helios Nanolab 600, FEI) was used to polish gold flakes down to the desired thickness of 30 nm. A current of 48 pA at an acceleration voltage of 30 kV was used and the sputtering rate was calibrated with assistance of AFM measurements beforehand.

To fabricate the EA antennas an ion current of 9.7 pA at an acceleration voltage of 30 kV was used. A MatLab script translates the binary matrix of the EA into a script for the FIB pattern generator, defining a set of polygons, which can be directly written by the FIB machine. This pattern was written in four paths, each path with a different direction (top to bottom, left to right, ...) to ensure the milled features being regularly shaped. Milling in only one direction leads to undesired redeposition effects. The pattern generator showed a substantially decreased milling depth for single holes of the EA pattern. We automatically adjusted the milling depth for single holes by a factor of 1.4, which was determined by empirical tests. The MatLab script therefore represents a "printer driver" for the FIB milling instrument.

5.6. Two-photon photo luminescence microscopy (TPPL)

The antennas where scanned through the focus of a pulsed laser with a center wavelength of $\lambda = 830$ nm (pulse length at sample position ≈ 900 fs, repetition rate 76 MHz, Coherent Inc. MIRA 900) focused via an oil immersion objective (Nikon, Plan APO 100x, NA=1.4). In the detection path, after a non-polarizing 50 :50 cube beam splitter, three filters (notch filter: OD > 6 at 830nm, Kaiser Optical System; two short pass filters: SP785 and SP680, Semrock) ensured the blocking of the direct reflection of the excitation laser. The remaining TPPL signal was focused onto a single photon counting module (PDM Series, Micro Photon Devices). The full setup is sketched in Appendix 6.9.

6. Appendix

6.1. FIB benchmarking

In order to determine geometrical restrictions of structures that are fabricated by focused ion beam milling, an 11×11 matrix test pattern was developed (see Fig. 4 left). The test pattern includes all relevant structural primitives, such as e.g. isolated gold islands, individual missing pixels (holes) and solid gold rims and corners. Figure 4 right shows an SEM picture of the structure with the final reproducible dimensions by means of FIB-milling. The holes have a diameter of 22 nm and their center-to-center distance is 30 nm.

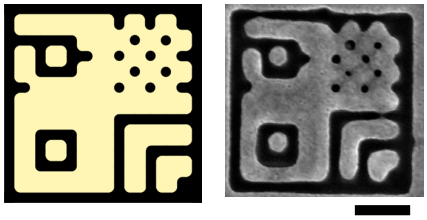

Fig. 4. 11×11 test pattern design for FIB benchmarking. Left: Sketch of geometry. Right: SEM picture of the resulting structure produced by FIB milling in 30 nm thick monocrystalline gold (scale bar = 100 nm).

6.2. Details of the evolutionary algorithm

One run of the evolutionary algorithm consists of consecutive generations containing 30 individuals each as depicted in the upper panel of Fig. 5. In the initialization step the very first generation $g = 1$ is built randomly, but with a given filling factor here $p_{fill} = 0.7$. This value

Optics EXPRESS

has proven beneficial for high fitness optical antennas [16]. All subsequent generations $g > 1$ are built from the best eight individuals of the preceding generation $g - 1$, their fitness being evaluated via FDTD simulations. Each new individual is generated via mutation with a probability of 0.4 or crossing with a probability of 0.6 (see Fig. 5 bottom). Mutation happens by switching each bit of the binary genome with a probability $p_{fl} = 0.01$, resulting in an average of $\sum_{i=0}^{n} p_{fl}(1 - p_{fl})^i = 0.7$ flips for $n = 120$ matrix elements ($11^2 - 1$; center spot is always free). Crossing mixes the genomes of two parents to generate a child. This mixing is realized in two different ways with equal probability, called 'linear' and 'spiral'. In the linear case the left part of an antenna A (painted blue in Fig. 5) up to a random matrix element is used and complemented with the right part of another antenna B (painted green). In the spiral case the inner part of an antenna A was complemented with the outer part of antenna B, and the size of the inner part was also determined randomly. A more detailed description together with a graphical explanation can be found in [16].

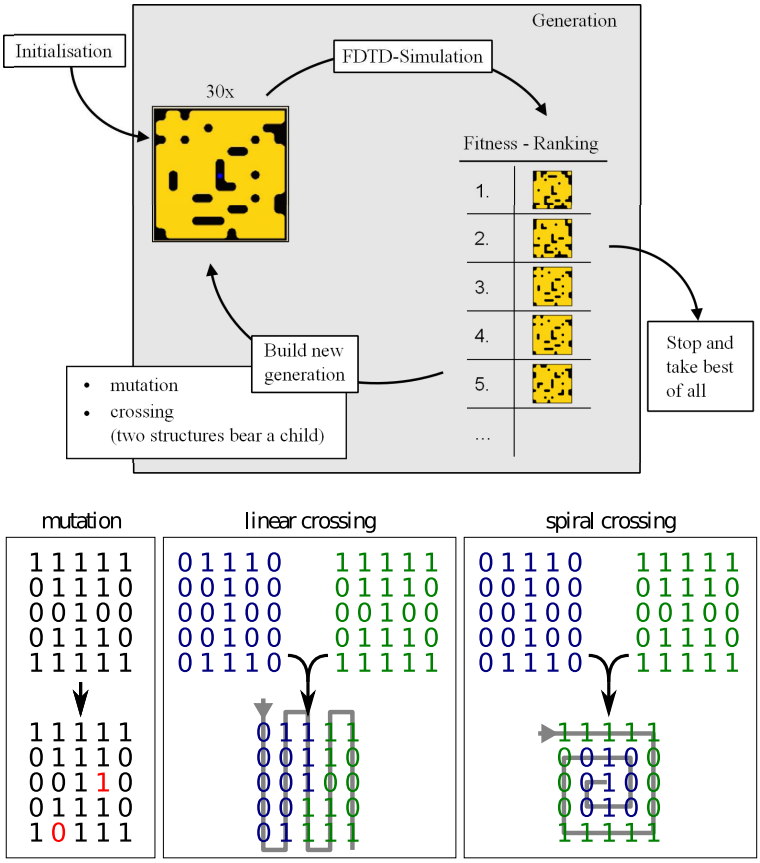

Fig. 5. Working principle of the evolutionary algorithm. Upper panel: Flowchart of the EA steps. Initially the fitness parameter of 30 random structures is evaluated by means of FDTD simulations. After ranking, the best eight are used for building the next generation by means of mutation and crossing. Bottom panel: Methods of inheritance. Left: Mutation changes single bits (red) with a given probability. Linear and spiral crossing mix the genome of two different parents (blue and green). Linear crossing combines left and right parts, while spiral crossing combines inner and outer parts of two parents.

The development of the fitness parameter within the present evolutionary algorithm as a function of the simulation number and the generation number is plotted in Fig. 6. The mean and

Optics EXPRESS

maximal fitness per generation do not increase monotonically since the algorithm avoids evaluations of redundant geometries. If a reproduction mechanism yields a already evaluated structure (or an mirrored, physically identical version of an already evaluated structure), it will be omitted and the reproduction will be repeated. Mutation introduces eventually new geometries into the gene pool of the EA and the algorithm is able to escape local fitness maxima in configuration space leading to a temporary reduction of the maximal fitness followed by an increase in fitness in later generations. The evolution was stopped after the previous set 60 generations, as the FEA surpasses the reference antenna in fitness. Full convergence of the evolution process cannot be ensured for complex optimization schemes, as there is no analytical way to calculate/estimate a maximum. However, the exponentially decreasing fitness gains for the final generations hint to the optimization being nearly optimal (albeit this could just be a local maximum in configuration space).

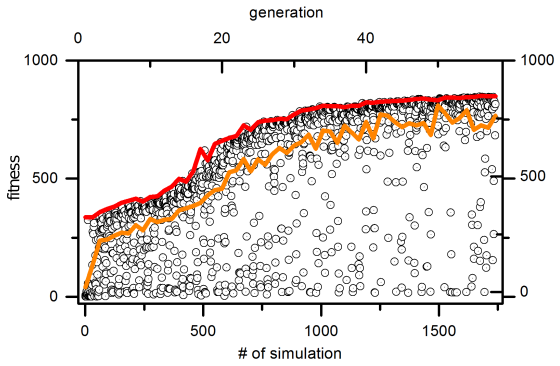

Fig. 6. Development of the fitness parameter for the EA discussed here. Each point denotes a single individual. Also the best fitness per generation (red) as well as the mean fitness per generation (orange) are shown.

6.3. *AFM measurement of antenna thickness*

The actual thickness of the fabricated structures has been measured by means of AFM (see Fig. 7). The pristine flake has a thickness of 48 ± 1 nm (area marked green) and the homogeneously ablated area, so-called polished area is reduced in height by 20 ± 1 nm (area marked blue). This results in a measured optical antenna thickness of 28 ± 2 nm, which is slightly less than the intended 30 nm.

The measurement was performed under ambient conditions using a tapping mode AFM operating at a resonance frequency of 240 – 280 kHz and a scanning rate of 0.2 Hz (DMLS scanning head, Nanoscope IIIa, Digital Instruments).

6.4. *Influence of reduced antenna height on the antenna resonance*

To assess the effect of a decreased thickness on the fitness of the evolutionary antennas, simulations of the six fabricated geometries were performed and the results plotted in Fig. 8. The fitness is reduced for thinner antennas, as the resonance shifts into the red [3], away from the wavelength of optimization. Except for antenna #5 the fitness hierarchy is maintained which can be explained with the spectra of all antennas (see Appendix 6.8). Antenna #5 is the only one with a relative blue shift with respect to the optimization wavelength, therefore being the only antenna optimized by the red shift.

Optics EXPRESS

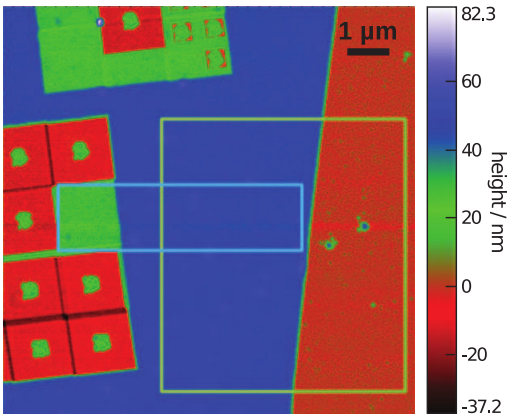

Fig. 7. AFM measurement used for the determination of optical antenna thickness. The green and blue marked areas were used to evaluate height histograms.

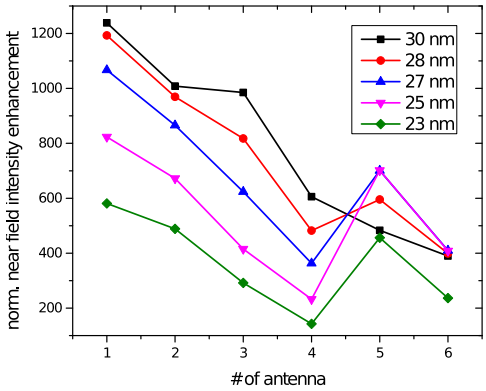

Fig. 8. Change in fitness of evolutionary antennas for different layer thicknesses. The best four antennas decrease in near-field intensity enhancement as their thickness is reduced, the last two behave not systematically.

6.5. TPPL signal of the reference antenna: numerical analysis

In addition to the evolutionary antennas, also the TPPL signal of the reference dipolar antenna [Fig. 2(a)] was evaluated numerically according to equation (1). Assuming a proportionality between the near-field intensity enhancement and the TPPL signal generated in the material of the antenna, the ratio:

$$r = \frac{|\mathbf{E}|^4(\mathbf{r_0})}{\int_{V_{antenna}} |\mathbf{E}|^4(\mathbf{r})\, dV} \tag{2}$$

should be comparable for the reference antenna and the fittest antenna since their near-field intensity enhancement is of the same order of magnitude. However, evaluating both reference and fittest antenna at $\lambda = 830$ nm yields $r_{reference}/r_{fittest} = 286.3$. This clearly shows that the TPPL signals cannot be used to compare antennas of vastly different gap geometry.

6.6. Influence of hole diameter on the antenna resonance

The fabrication of the holes and lines needed to realize the evolutionary antennas has an uncertainty of ±1 nm. The influence of such a deviation in the geometry on the fitness all six

Optics EXPRESS

fabricated antennas has been simulated by increasing as well as decreasing all hole diameters by 1 nm. The results in Fig. 9 show nearly no influence of this parameter on the relative fitness hierarchy. The large absolute fitness increase for smaller hole sizes – which is about 100 nm^{-1} – originates from the enhanced capacitive coupling in the center gap, when the accumulating charges are less separated. This observation also explains the error bar within the TPPL measurements for all structures.

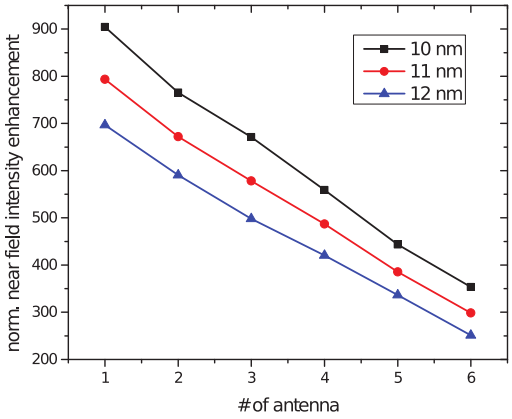

Fig. 9. Change in fitness of evolutionary antennas dependent on the hole diameter / line width. As the width gets smaller, the near-field intensity enhancement increases by a large margin.

6.7. *TPPL evaluation with central illumination only*

The numerical results of the evolutionary antennas are obtained with perfectly central illumination, however, the experimental TPPL data are retrieved by scanning a laser beam over the antennas. Contrary to the evaluation method of the main text, where the complete TPPL signal per antenna is summed up, here only the central 3x3 part of the TPPL signal of each antenna is summed up for better comparison with the numerical results. Therefore, the very center of all pixels of one antenna signal spot with a value above a noise threshold of 5 counts are weighted to determine the antenna signal center. The central TPPL values are adjusted to overlap with the previous data (see green data points in Fig. 10).

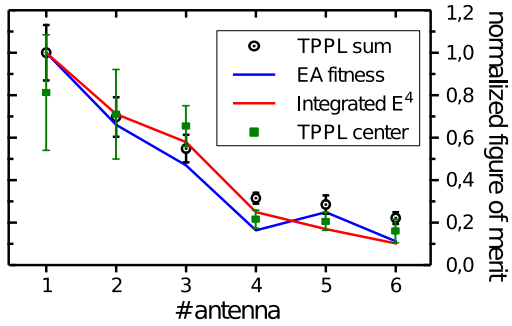

Fig. 10. Reproduction of Fig. 3(c), however, with additional data evaluated from the very center of the TPPL spots only (green). More details in text.

It is clearly visible that the error increases. Still, within the error margin the central TPPL data matches to the numerical values of the antennas TPPL signal (red line).

Optics EXPRESS

6.8. Correction of numerical TPPL due to emission shaping

If an optical antenna shows several resonances, the lower wavelength modes possibly lead to an enhancement and shaping of the TPPL signal [28].To assess the influence of the evolutionary antenna emission spectrum on the TPPL emission, their near-field intensity integrated over the antenna volume was simulated (see Fig. 11(a)).

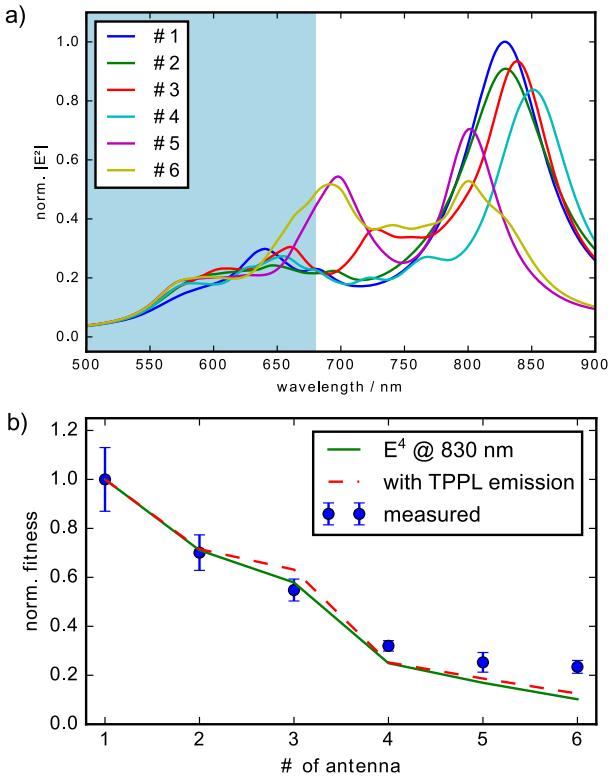

Fig. 11. a) Spectrum of the field inside the material of the evolutionary antennas, integrated over their respective volumes. b) Approximative corrections to the numerical TPPL signal due to TPPL emission enhancement. More details in text.

Due to memory restrictions of our simulation cluster we were only able to simulate the broadband spectrum in a 2D plane located 2 nm above the ITO podest, the antennas sit on. There the mode fields have the largest intensity. Since the antenna thickness is only 28 nm we can savely assume the mode field pattern not to change along the z-axis, perpendicular to the antenna plane.

From the data shown in Fig. 11 the spectral range between 500 and 680 nm was integrated to retrieve a weighting factor for the numerical TPPL data as presented in Fig.3(c). The result is shown in Fig. 11(b): the blue dots and the solid green line are the experimental and numerical TPPL data from Fig.3(c) respectively. The red dashed line shows the data weighted by the TPPL emission spectrum. The changes are minor, but the trend for the last two antennas is correct.

6.9. Experimental setup

The optical setup is a home-built confocal microscope (see Fig. 12). The antennas where excited using a pulsed laser at a center wavelength of $\lambda = 830$ nm (pulse length 300 fs, repetition rate 76 MHz, Coherent Inc. MIRA 900) attenuated to a power of 80 μW focused via an oil immersion objective (Nikon, Plan APO 100x, NA=1.4). The detection path - separated by a non-polarizing 50:50 cube beam splitter - three filters (notch filter: OD > 6 bei 830nm, Kaiser Optical System;

Optics EXPRESS

two short pass filters: SP785 and SP680, Semrock) ensured the blocking of the direct reflection of the excitation laser and the detection of wavelengths. The signal was focused onto a single photon counting module (PDM Series, Micro Photon Devices).

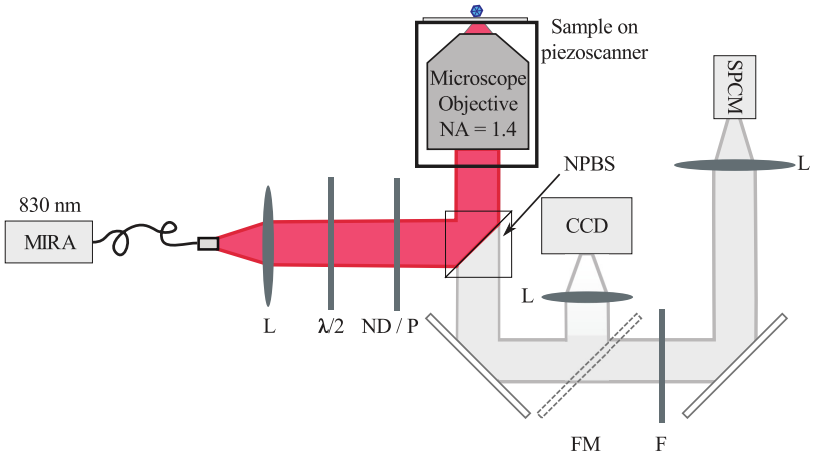

Fig. 12. Experimental setup for TPPL microscopy. L: lens; ND/P: neutral density filter and polarizer; NPBS: non-polarizing beam-splitter; F: filters; FM: flip mirror. For further information see text.

Funding

Deutsche Forschungsgemeinschaft (DFG) (HE5648/1-1).

Acknowledgments

The authors wish to thank J. Kern and S. Grossmann for fruitful discussions.